Nonlinear Response of Atmospheric Blocking to Early Winter Barents–Kara Seas Warming: An Idealized Model Study

XIAODAN CHEN,[a,b] DEHAI LUO,[b] YUTIAN WU,[c] ETIENNE DUNN-SIGOUIN,[d,e] AND JIAN LU[f]

[a] *Department of Atmospheric and Oceanic Sciences, Institute of Atmospheric Sciences, Fudan University, Shanghai, China*
[b] *CAS Key Laboratory of Regional Climate-Environment for Temperate East Asia, Institute of Atmospheric Physics, Chinese Academy of Sciences, and University of Chinese Academy of Sciences, Beijing, China*
[c] *Lamont-Doherty Earth Observatory, Columbia University, Palisades, New York*
[d] *Geophysical Institute, University of Bergen, Bergen, Norway*
[e] *Bjerknes Centre for Climate Research, Bergen, Norway*
[f] *Atmospheric Sciences and Global Change Division, Pacific Northwest National Laboratory, Richland, Washington*

(Manuscript received 26 September 2019, in final form 9 December 2020)

ABSTRACT: Wintertime Ural blocking (UB) has been shown to play an important role in cold extremes over Eurasia, and thus it is useful to investigate the impact of warming over the Barents–Kara Seas (BKS) on the behavior of Ural blocking. Here the response of UB to stepwise tropospheric warming over the BKS is examined using a dry dynamic core model. Nonlinear responses are found in the frequency and local persistence of UB. The frequency and local persistence of the UB increase with the strength of BKS warming in a less strong range and decrease with the further increase of BKS warming, which is linked to the UB propagation influenced by upstream background atmospheric circulation. For a weak BKS warming, the UB becomes more persistent due to its less westward movement associated with intensified upstream zonal wind and meridional potential vorticity gradient (PV_y) in the North Atlantic mid-high latitudes, which corresponds to a negative height response over the North Atlantic high latitudes. When BKS warming is strong, a positive height response appears in the early winter stratosphere, and its subsequent downward propagation leads to a negative NAO response or increased Greenland blocking events, which reduces zonal wind and PV_y in the high latitudes from North Atlantic to Europe, thus enhancing the westward propagation of UB and reducing its local persistence. The transition to the negative NAO phase and the retrogression of UB are not found when numerically suppressing the downward influence of weakened stratospheric polar vortex, suggesting a crucial role of the stratospheric pathway in nonlinear responses of UB to the early winter BKS warming.

KEYWORDS: Atmosphere; Arctic; Asia; Europe; Blocking; Nonlinear dynamics

1. Introduction

In the recent two decades, the Barents–Kara Seas (BKS) show the most pronounced Arctic warming in the cold season in observations (Cohen et al. 2014; Shepherd 2016) and climate simulations (Sun et al. 2016; Ogawa et al. 2018). The BKS warming shows bottom-heavy warming extending into the midtroposphere in reanalysis (e.g., Screen and Simmonds 2010; Walsh 2014), coupled model simulations with the historical forcing (Smith et al. 2017), and representative concentration pathways (e.g., Deser et al. 2015; Wu and Smith 2016; Sun et al. 2018; Dai and Song 2020). The era of BKS surface temperature rise related to sea ice concentration (SIC) decline coincides with an increase in cold extremes over midlatitude Eurasia (e.g., Overland et al. 2011, 2015; Outten and Esau 2012; Liu et al. 2012; Francis and Vavrus 2012). The causality between the midlatitude cold anomalies and Arctic warming or sea ice loss has attracted much scientific interest (e.g., Vihma 2014; Cohen et al. 2014, 2020; Overland et al. 2016). The interest is driven by the emerging evidence that BKS warming or sea ice loss dynamically forces the mid–high-latitude atmospheric circulation on interannual and subseasonal time scales (e.g., Honda et al. 2009; Inoue et al. 2012; Tang et al. 2013; Kim et al. 2014; Cohen et al. 2014; Luo et al. 2016; Yao et al. 2017; Luo et al. 2018, 2019a). However, enormous disagreement exists among modeling studies on whether Arctic sea ice affects the mid–high-latitude circulations and temperatures (e.g., Mori et al. 2014, 2019; Kug et al. 2015; Sun et al. 2016; Blackport et al. 2019; Peings 2019; Xu et al. 2019; Dai and Song 2020). The divergence could be partially owing to different magnitudes of Arctic sea ice loss (Overland et al. 2016; Screen et al. 2018) because the mean-state atmospheric circulation response to different magnitudes of Arctic sea ice loss is highly nonlinear (Petoukhov and Semenov 2010; Peings and Magnusdottir 2014; Semenov and Latif 2015).

Ural blockings (UBs), persistent anticyclonic anomalies around the Ural Mountains, significantly influence cold anomalies over Eurasia by cold air advection, particularly for persistent and quasi-stationary UBs (Luo et al. 2016; Yao et al. 2017; Chen et al. 2018). The importance of UBs in the warm BKS–cold Eurasia pattern has been widely suggested (e.g., Mori et al. 2014; Overland et al. 2015; Luo et al. 2016, 2018, 2019a; Tyrlis et al. 2019, 2020; Siew et al. 2020). It has been

Supplemental information related to this paper is available at the Journals Online website: https://doi.org/10.1175/JCLI-D-19-0720.s1.

Corresponding author: Dehai Luo, ldh@mail.iap.ac.cn

Publisher's Note: This article was revised on 3 March 2021 to correct a typographical error in an equation in the first paragraph of section 4a.

DOI: 10.1175/JCLI-D-19-0720.1

© 2021 American Meteorological Society. For information regarding reuse of this content and general copyright information, consult the AMS Copyright Policy (www.ametsoc.org/PUBSReuseLicenses).

Brought to you by UNIVERSITETSBIBLIOTEKET I | Unauthenticated | Downloaded 03/09/22 08:50 AM UTC

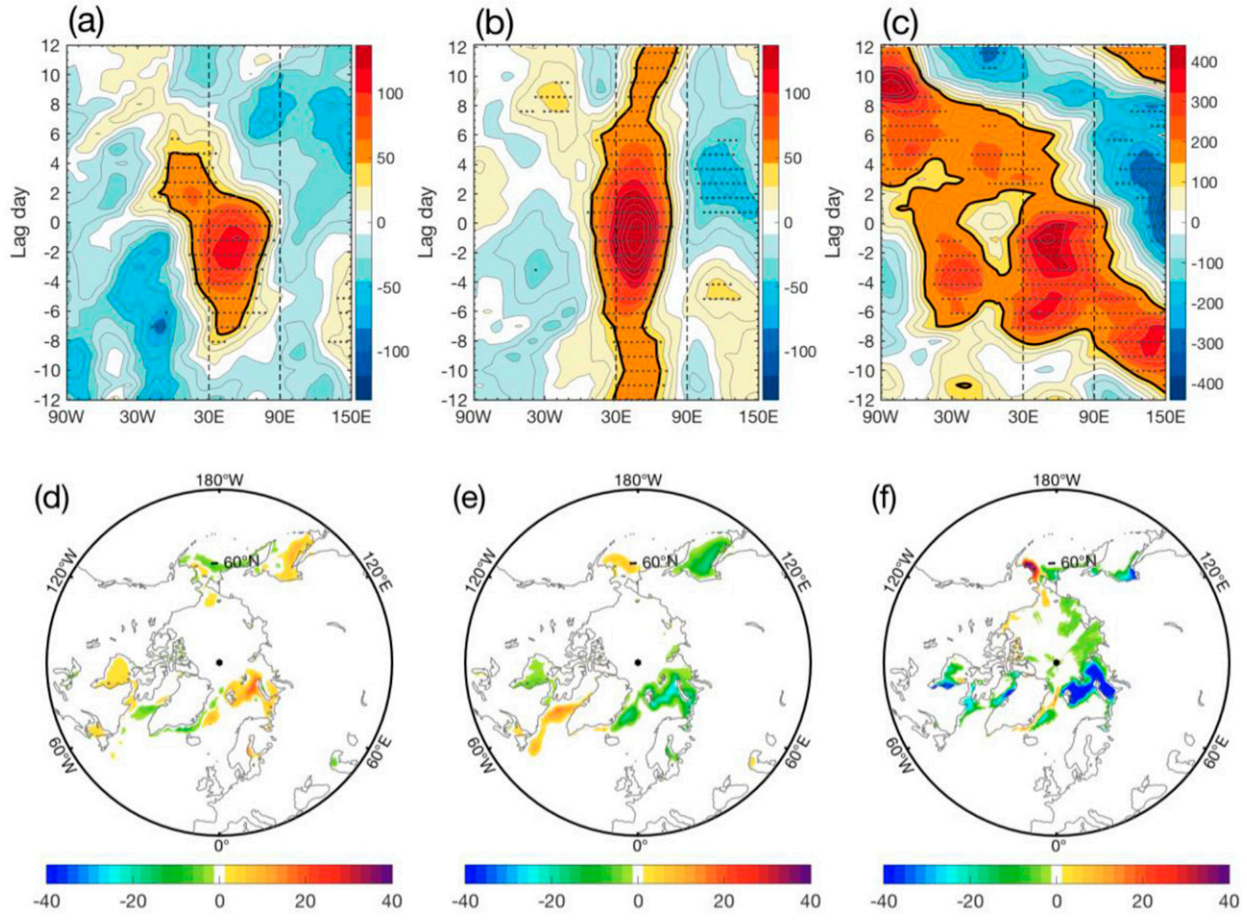

FIG. 1. Time–longitude evolution of composited daily Z500 anomalies [color shadings; contour interval (CI) = 20 gpm] averaged over 50°–75°N and background SIC anomalies (%) for the UB events with (a),(d) high, (b),(e) low, and (c),(f) extreme low background BKS SIC in 2011 winter. The UB events with high (low) background SIC are defined when the background BKS SIC anomalies is above (below) 0%, and UB events with extreme low BKS SIC are defined when the background BKS SIC anomalies are below −15%, where SIC anomalies are calculated relative to the climatology for 1979–2001. Lag 0 denotes the peak day and negative lag days refer to days prior to the peak of UB event. The SIC averaged from lag −30 to lag −10 is defined as background SIC for UB events. Black thick line denotes the value of 50 gpm in (a) and (b) and denotes the value of 160 gpm in (c). Stippling in (a)–(c) and shading in (d)–(f) denote the statistically significant region at the 95% confidence level using the Student's *t* test.

hypothesized that the BKS sea ice loss drives increased Ural blocking (e.g., Luo et al. 2016; Yao et al. 2017; Overland et al. 2016; Cohen et al. 2020). In Figs. 1a, 1b, 1d, and 1e, persistent and quasi-stationary UBs are associated with less SIC over the BKS, which is in line with the results of Yao et al. (2017) and Luo et al. (2018). However, a recent UB event in December 2011 appears to move westward rapidly when BKS SIC is extremely low (Figs. 1c,f). This implies that the extremely low BKS SIC seems to suppress the local persistence or quasi-stationarity of UB, suggesting that there is a nonlinear relationship between the extent of BKS SIC and UB. Although Luo et al. (2016) and Yao et al. (2017) found that the BKS warming with less BKS SIC can increase the persistence and quasi-stationarity of UB, how the varying BKS warming, including extreme BKS warming with extremely low BKS SIC, influences the UB is not clarified in previous studies. Thus, it is useful to investigate the nonlinear response of UB to the different extent of BKS SIC or varying BKS warming in the present study. To address this question, we use a BKS warming instead of BKS SIC decline when a dry dynamical core model is used because the BKS SIC decline corresponds to BKS warming. Using this dry dynamical core model with a prescribed BKS warming, the variations of wintertime UB in response to different strengths of BKS warming are examined in this paper.

In this study, many new findings are revealed. It is found that the UB shows a nonmonotonic and nonlinear variation in response to different strengths of BKS warming. When BKS warming is less strong, the UB tends to be more persistent and quasi-stationary as the strength of BKS warming increases. In this case, the stratospheric process barely affects tropospheric circulation. Conversely, when BKS warming is strong, the downward influence of the stratosphere generates a negative North Atlantic Oscillation (NAO^-) response and plays an important role in the change of UB, specifically enhancing its

Brought to you by UNIVERSITETSBIBLIOTEKET I | Unauthenticated | Downloaded 03/09/22 08:50 AM UTC

westward movement and reducing its persistence. This study is the first report of nonlinear UB response to BKS warming via stratospheric processes.

This paper is organized as follows. In section 2, we describe the blocking identification method, the numerical model, and the experimental setup. Section 3 presents the model results about the UB changes in frequency, local persistence, and movement in response to different strengths of BKS warming. The linkage between the UB change and the background circulation response is examined in section 4. Section 5 discusses the influence of the stratospheric processes associated with BKS warming on tropospheric circulation and UB. Conclusions and discussion are presented in section 6.

2. Method, model, and experiments

a. Blocking identification

As noted by Luo et al. (2016), BKS warming or SIC decline can significantly influence the Ural blocking. Thus, in this study we use a hybrid two-dimensional blocking index of Dunn-Sigouin et al. (2013), which considers the change of the blocking size.

Before applying the blocking identification algorithm, the deviation of the 500-hPa geopotential height (Z500) from its climatological mean and seasonal cycle is considered as the Z500 anomaly for each experiment. We calculate the standard deviation (STD) for the daily Z500 anomalies north of 30°N during a 3-month moving window. If a horizontal area consisting of instantaneous Z500 anomalies greater than 1.5 STDs has a minimum scale of 2.5×10^6 km^2, it may be identified as an instantaneous blocking area. Next, a reversal of Z500 meridional gradient is required on the equatorward side of maximum Z500 anomalies within the instantaneous blocking area. The instantaneous blocking areas in two successive days are considered as belonging to one blocking if their overlap is greater than 50%. Otherwise, they are considered as belonging to different blockings. A blocked day at a grid point is defined when this point is within the instantaneous blocking area of a blocking. Winter blocking frequency at each point is calculated in terms of the percentage of blocked days in total days of winter [December–February (DJF)] at this point. A blocking event is identified if the daily maximum Z500 anomaly of instantaneous blocking areas persists at least five days in a region (30°–90°E and 50°–75°N for Ural blocking or 90°–30°W and 50°–75°N for Greenland blocking). The duration of the blocking event is defined as the total days of the maximum Z500 anomaly of instantaneous blocking areas staying within the region.

b. Model and its blocking representation

The numerical model we used here is a dry dynamical core model developed by Wu and Reichler (2018, hereafter WR18) based on the primitive equations of motion and temperature. In this model, a Newtonian term is relaxed to the target radiative equilibrium temperature, and the Rayleigh damping is used to represent boundary friction. The WR18 model has a realistic topography and a zonally asymmetric equilibrium temperature profile obtained from the ERA-40 reanalysis (1958–2001) using an iterative approach by Chang (2006). We run the model with a seasonal cycle, a horizontal resolution of T42, and 40 vertical levels from the surface to 0.01 hPa. Outputs of the default run show that the DJF-mean wind and stationary waves are close to the climatological states in ERA-Interim reanalysis (Dee et al. 2011) during 1979–2001 (Fig. S1 in the online supplemental material).

We compare the winter blocking frequency in the WR18 model, ERA-Interim, and 18 models in phase 6 of the Coupled Model Intercomparison Project (CMIP6) to indicate that the WR18 model can capture the structure and characteristics of blocking in the Northern Hemisphere. The description of the CMIP6 models is given in supplemental Table S1. As shown in Fig. 2a, the WR18 model shows an acceptable ability to simulate the blocking frequency around the Ural Mountains, compared with many state-of-the-art CMIP6 models we analyzed here. The event duration and frequency of UB events in ERA-Interim can be well reproduced by the WR18 model as seen from Fig. 2b, thus suggesting that there are many similarities between simulated and observed UBs in many aspects including dynamical processes. However, a large difference with the observed one is that the WR18 model overestimates the blocking frequency over Arctic high latitudes, especially over BKS (Figs. 2c,d), but it can crudely simulate the blocking frequency over the Ural region although slightly lower than the observed. Perhaps such an Arctic high-latitude difference is attributable to the northeastward extension of the North Atlantic jet and the weak Eurasian stationary ridge in the WR18 model (Fig. S1). Even so, it is feasible to use the WR18 model to examine how different strengths of BKS warming affect winter UBs because our emphasis is mainly placed on the behavior (changes in frequency, duration or local persistence, and movement) of UB.

c. Experiments

We put an additional heating rate into the radiative equilibrium temperature profile with an approach following previous studies (e.g., Zhang et al. 2018b):

$$\frac{\partial T}{\partial t} = \cdots k_T^{-1}\{T - [T_{\mathrm{eq}}(\lambda,\phi,\sigma,t) + T_{\mathrm{eq}}^{\mathrm{BKS}}(\lambda,\phi,\sigma,t)]\}, \quad (1)$$

where k_T is the Newtonian relaxation time, λ is longitude, ϕ is latitude, σ is sigma level, t is the time in month, T_{eq} is the control radiative equilibrium temperature profile varying with month, and $T_{\mathrm{eq}}^{\mathrm{BKS}}$ is the perturbed radiative equilibrium temperature profile representing BKS warming. Here $T_{\mathrm{eq}}^{\mathrm{BKS}}$ is expressed in an analytical form:

$$T_{\mathrm{eq}}^{\mathrm{BKS}} = \begin{cases} T_{\mathrm{Max}}^{\mathrm{BKS}} \times \cos^a\left[\dfrac{(\phi-\phi_0)}{p}\right] \times \sin^b\left(\dfrac{\lambda}{q}\right) \times e^{c(\sigma-1)} \times \dfrac{1}{2}\left\{\cos\left[\dfrac{(t-t_0)2\pi}{12}\right]+1\right\}, \text{ for } \phi_S \le \phi \le \phi_N, \lambda_W \le \lambda \le \lambda_E, 1 \le t \le 12 \\ 0, \text{ otherwise} \end{cases}, \quad (2)$$

Brought to you by UNIVERSITETSBIBLIOTEKET I | Unauthenticated | Downloaded 03/09/22 08:50 AM UTC

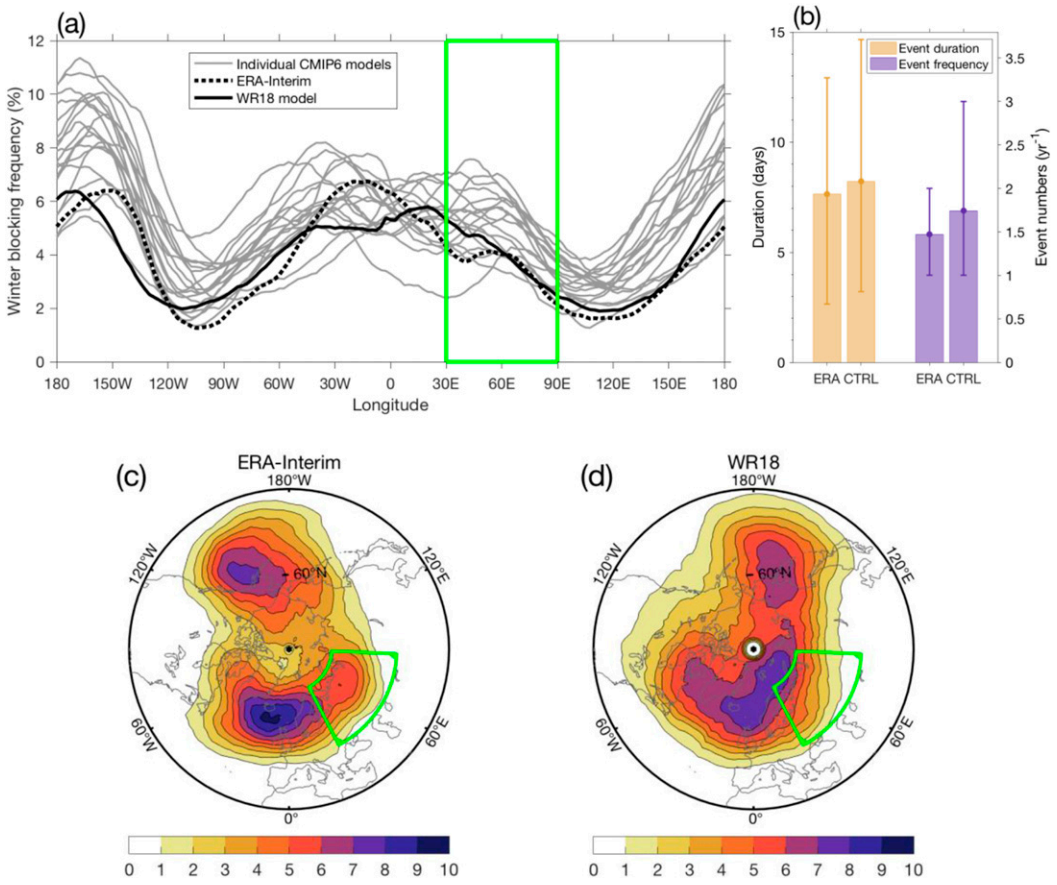

FIG. 2. (a) Winter blocking frequency averaged from 50° to 75°N for ERA-Interim (black dotted line), the WR18 model (black solid line), and individual CMIP6 models (gray lines). The green box highlights the longitudes around the Ural Mountains (30°–90°E). (b) Duration and frequency of the UB event for ERA-Interim and CTRL (interquartile ranges are given by whiskers). Also shown is winter blocking frequency (contours and colors; %) for (c) ERA-Interim reanalysis (1979–2000) and (d) WR18 (50 winters). The green box denotes the region around Ural Mountains (30°–90°E, 50°–75°N).

where $\phi_S = 65°\text{N}$, $\phi_N = 90°\text{N}$, $\lambda_W = 0°$, $\lambda_E = 120°$, $p = \max[(\phi_N - \phi_o)/90°, (\phi_0 - \phi_S)/90°]$, $q = (\lambda_E - \lambda_W)/180°$, and $t_0 = 11$, indicating that the BKS heating is maximized in November at the BKS surface and remains relatively strong in December and January (see Fig. 3), which is referred to as the early winter BKS warming hereafter. In Eq. (2), $T_{\text{Max}}^{\text{BKS}}$ is the maximum heating strength, and a, b, and c describe the zonal extent, meridional extent, and vertical extent of the idealized heating, respectively; we set $a = 4$, $b = 2$, and $c = 3$ following Wu and Smith (2016) and Zhang et al. (2018a). When altering the value of c from 3 to 5, the heating strength decays faster with height, representing a shallower BKS warming (Fig. S2). Some results of shallower warming simulations are shown in the supplemental material.

To examine the response of UB and its sensitivity to the strength of BKS warming, we only alter the value of $T_{\text{Max}}^{\text{BKS}}$ in Eq. (2) in our experiments. Eight perturbation experiments are performed with $T_{\text{Max}}^{\text{BKS}} = 25$, 50, 75, 100, 150, 175, and 200 K, which are referred to as T25, T50, T75, T100, T125, T150, T175, and T200, respectively. The relaxation time scale is about 25 days near the surface of the BKS (see Jucker et al. 2014), corresponding to the maximum surface heating rates ranging from 1 to 8 K day^{-1} in our perturbation experiments (Fig. 3a). For comparison, we define $T_{\text{Max}}^{\text{BKS}} = 0$ as the control experiment (CTRL). Deviations of the warming experiment from CTRL are defined as the responses to BKS warming. In our subsequent discussions, a positive (negative) Z500 response is defined as the positive (negative) Z500 anomaly in response to BKS warming compared to CTRL. The BKS warming shows maximal heating over the BKS surface (Fig. 3b) that decays with height and extends to the midtroposphere for T125, T150, T175, and T200 (Fig. 3c), resembling the bottom-heavy Arctic warming with deep vertical structures in observations (e.g., Screen and Simmonds 2010; Walsh 2014) and fully coupled simulations (e.g., Deser et al. 2015; Smith et al. 2017; Dai and Song 2020). The imposed heating for T50 (T150) experiment approximately represents the observational BKS warming during 2000–10 (2011–18) (Fig. S3). During the winter of 2011, when the extremely low BKS sea ice and west-shifting UB appears, BKS warming also exhibits a deep vertical extent

Brought to you by UNIVERSITETSBIBLIOTEKET I | Unauthenticated | Downloaded 03/09/22 08:50 AM UTC

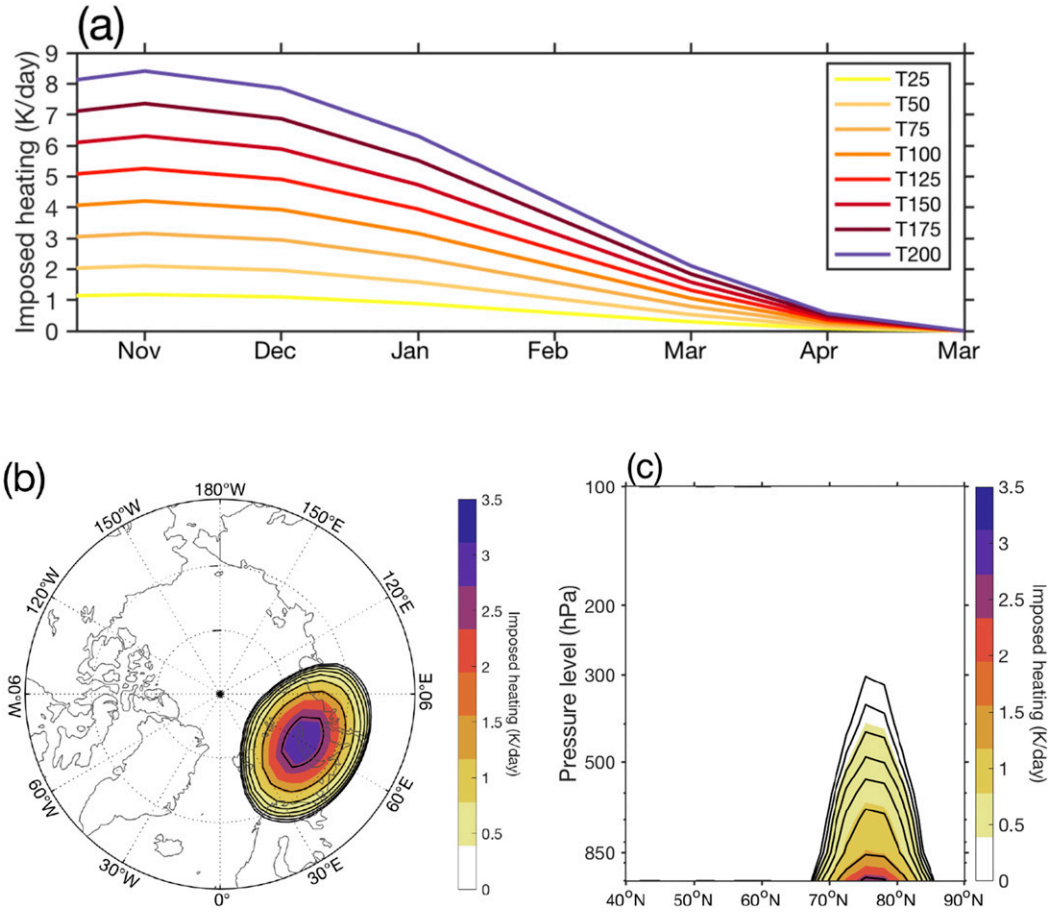

FIG. 3. (a) Temporal evolution of the maximum strength of heating imposed in Barents–Kara Seas for each experiment. (b),(c) Color shadings represent horizontal (at the lowest layer) and vertical–latitude (averaged over 30°–90°E) distributions, respectively, of a DJF-mean imposed heating (K day^{-1}) for T100, and the black line represents the 0.8 (K day^{-1}) contour for the imposed heating in each experiment.

(Fig. S3). Thus, the strong and deep BKS warming experiments may help us understand the mechanisms of westward-shifting UBs associated with strong BKS warming.

To separate the influences of the tropospheric process and stratospheric process on the overall mean-state response and blocking response, we conduct two additional sets of experiments with a nudging method (e.g., Simpson et al. 2013; Nakamura et al. 2016; Wu and Smith 2016; Zhang et al. 2018a,b). The nudging method we used is the same as that in Wu and Smith (2016) but with a nudging time scale of 6 h. The first set has three nudging experiments with BKS warming the same as in T50, T100, and T150, respectively, but their zonal-mean stratospheric circulations are all nudged toward CTRL. More specifically, we first calculate the multiyear climatology of CTRL outputs on 365 calendar days as a reference state. Then we run the model with BKS warming and nudge the zonal-mean vorticity, divergence, and temperature toward the reference state on the same calendar day at every time step in the stratosphere. In this way, the stratospheric influence on the troposphere is suppressed, leaving the tropospheric process, which mainly includes the adjustment of tropospheric atmospheric circulation to diabatic heating. Thus, according to the warming strength change, the first set of nudging experiments are referred to as T50_T, T100_T, and T150_T, where the capital T denotes the tropospheric pathway only.

The second set includes three nudging experiments without BKS warming, in which the zonal-mean stratospheric circulations are nudged toward the multiyear climatology of T50, T100, and T150 on 365 calendar days, respectively. In this case, the tropospheric response only results from the downward influence of the imposed stratospheric changes related to BKS warming. Accordingly, these experiments are referred to as T50_S, T100_S, and T150_S, where the capital S denotes the stratospheric effect only. In addition, we conduct a run without BKS warming and nudge its zonal-mean stratosphere toward the seasonal climatology of CTRL. This run is referred to as CTRL_N, where the capital N denotes nudging. The difference between CTRL_N and CTRL represents the biases caused by nudging (Nakamura et al. 2016). We will analyze the deviation of the nudging experiments from CTRL_N instead of CTRL to avoid the nudging biases.

Brought to you by UNIVERSITETSBIBLIOTEKET I | Unauthenticated | Downloaded 03/09/22 08:50 AM UTC

TABLE 1. The experiment design we analyzed in this model study.

Experiment name	Idealized heating	Nudging description
CTRL	—	—
T25, T50, T75, T100, T125, T150, T175, T200	As in Eq. (2) with maximum heating strength of 25, 50, 75, 100, 125, 150, and 200 K, respectively	—
T50_T, T100_T, T150_T	As in Eq. (2) with maximum heating strength of 50, 100, and 150 K, respectively	Nudging the stratospheric zonal mean state toward CTRL
T50_S, T100_S, T150_S, and CTRL_N	—	Nudging the stratospheric zonal mean state toward T50, T100, T150, and CTRL, respectively

Table 1 lists the experiments we will analyze in the following sections. Each experiment is integrated for 55 years, and the last 50 winters are used to calculate the equilibrium results.

3. Nonlinear blocking response to BKS warming

To examine the impact of the different strengths of BKS warming on blocking, we first calculate the difference of winter blocking frequency between BKS warming experiments (T25, T50, T75, T100, T125, T150, T175, T200) and CTRL (Fig. 4). It is found that the blocking frequency over the Eurasian–Atlantic sector varies with the strength of BKS warming. A positive response of blocking frequency appears over the Ural region (green box) with weak BKS warming (T25) and increases with the strengthening of BKS warming from T25 to T50 (Figs. 4a,b). Thereafter, it extends westward and shifts gradually to the North Atlantic or Greenland when the BKS further warms, eventually leading to a decreased blocking frequency over the Ural region and an increased blocking frequency over Greenland or North Atlantic in the extreme warm cases (Figs. 4c–h). These results also hold in the experiments with shallower BKS warming (Fig. S4).

To understand the varying response of blocking frequency, we show the event number per winter, the event duration, and the domain-averaged blocking frequency over the Ural region (Fig. 5a) and Greenland region (Fig. 5b) as a function of BKS warming in these experiments. We find that the event number of UBs (gray bar in Fig. 5a) is about 1.6 events per winter and almost independent of BKS warming strength, whereas the duration of UB (blue line in Fig. 5a) shows a nonmonotonic variation with the strengthening of BKS warming. It increases from about 8 days in CTRL to about 10 days in T50, and then it decreases with the further warming BKS until less than 7 days in T200. The variation of the UB duration resembles the variation of the domain-averaged UB frequency (red line in Fig. 5a), implying that the change of the UB frequency in response to different strengths of BKS warming is mainly attributed to the change in event duration rather than event number. In contrast, the duration of the Greenland blocking (GB) event (blue line in Fig. 5b) does not significantly depend on the strength of BKS warming, but the event number of GBs (gray bar in Fig. 5b) first decreases slightly and then increases with the strength of BKS warming, showing a change in a similar way to the domain-averaged blocking frequency (red line in Fig. 5b). Thus, different from UB, the variation of the blocking frequency over Greenland is mainly attributed to the change in GB event number rather than its duration. The above results decompose the change in blocking frequency in Fig. 4 into event duration and event number changes, indicating that while a less strong BKS warming favors long-lived UB events, a strong BKS warming tends to shorten the event duration of UB but increase the event numbers of GB. Similar results are found when using different duration thresholds in blocking identification (Fig. S5).

Next, we consider T50, T100, and T150 as the weak, medium, and strong cases of BKS warming. We show the time–longitude evolution of daily Z500 anomalies averaged over 50°–75°N for UB events in CTRL, T50, T100, and T150 (Figs. 6a–d), where lag 0 denotes the peak day of UB. In T50, the UB has less westward movement and hence has a longer duration within the Ural region (Fig. 6b) relative to CTRL (Fig. 6a). In T100 (Fig. 6c) and T150 (Fig. 6d), UB becomes less persistent and shows a stronger westward propagation than CTRL. In Fig. 6e, we further show the time–longitude variations of the maximum daily Z500 anomalies for UB events in CTRL and all BKS warming experiments. It is found that UB propagates westward in all cases, but the speed of the propagation depends on the strength of BKS warming. The UB events in T50 and T75 become stationary and almost stay over the Ural region during its entire life cycle, resulting in the longer local persistence over the Ural region. However, when BKS warming is stronger (from T100 to T200), the westward propagation of UB outside the Ural region becomes faster. This leads us to conclude that the UB propagation shows a strong nonlinear behavior in response to the stepwise increase of BKS warming. We also find that the notable westward propagation of UB mainly takes place west of 30°E, suggesting that the background condition in the upstream side of 30°E may play an important role in the westward propagation of UB.

4. Physical mechanism of nonlinear responses of Ural blocking

Given the importance of the change in blocking propagation, next we will use the phase speed of blocking to diagnose the mechanism of the change in blocking propagation under different BKS warming conditions.

Brought to you by UNIVERSITETSBIBLIOTEKET I | Unauthenticated | Downloaded 03/09/22 08:50 AM UTC

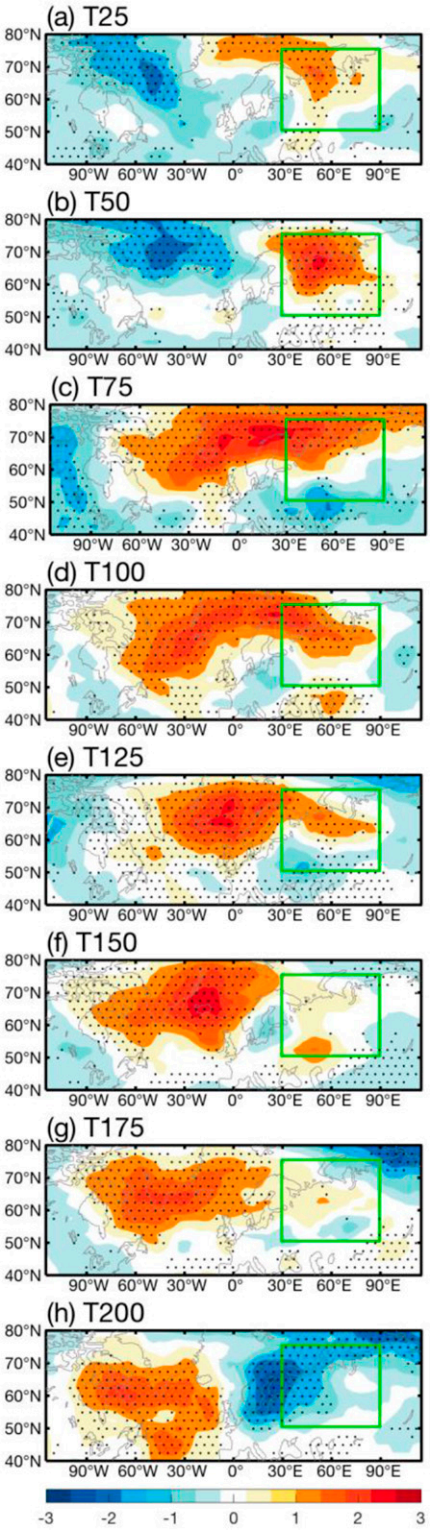

FIG. 4. Spatial distributions of the DJF-mean blocking frequency response to different strength of BKS warming for (a) T25, (b) T50, (c) T75, (d) T100, (e) T125, (f) T150, (g) T175, and (h) T200 experiments minus CTRL (color shadings; %, the percentage of blocked days in winter). The green box denotes the Ural region (30°–90°E, 50°–75°N). Stippling denotes the statistically significant region at the 95% confidence level using the Student's t test.

a. Nonlinear phase speed of blocking

Yeh (1949) considered the atmospheric blocking as a linear Rossby wave packet. In this theory, the propagation or movement of blocking can be interpreted as the time variation of the position of its maximum anticyclonic anomaly. In a slowly varying zonal basic flow, the phase speed of linear barotropic Rossby wave can be obtained as

$$C_P = U - \frac{PV_y}{k^2 + m^2 + F}, \tag{3}$$

where U and $\mathrm{PV}_y = \zeta_y + \beta + FU$ are the zonal basic-state wind and the meridional gradient (PV_y) of potential vorticity of the background circulation respectively, $\zeta_y = \partial\zeta/\partial y$ is the meridional gradient of background relative vorticity ζ, β is the meridional gradient of the Coriolis parameter at a given reference latitude, k and m are zonal and meridional wavenumbers, respectively, and $F = (1/R_d)^2$, where L is the characteristic length ($\sim$1000 km) and $R_d \sim 1000$ km is the radius of Rossby deformation. The parameters k, m, and F are approximate constants, because the horizontal size and geographical location of the UB barely change among the experiments (Fig. S6).

Because the linear phase speed C_P in Eq. (3) is positive for a small-amplitude wave in a relatively strong westerly wind, it cannot explain why blockings with large amplitudes propagate westward because it ignores the effect of the blocking amplitude on the phase speed of blocking (Luo 2000, 2005; Luo et al. 2019b). To better describe the blocking propagation, a nonlinear phase speed formula that takes the large amplitude of blocking into account has been proposed based on the nonlinear multiscale interaction model of blocking by Luo et al. (2019b). This nonlinear phase speed C_{NP} of blocking can be expressed as

$$C_{\mathrm{NP}} = C_P + C_N = U - \frac{\mathrm{PV}_y}{k^2 + m^2 + F} - \frac{\delta_N M_0^2}{2k\mathrm{PV}_y}. \tag{4}$$

The term $C_N = -\delta_N M_0^2/(2k\mathrm{PV}_y)$ represents the nonlinear part of C_{NP} and reflects the blocking amplitude–induced phase speed (Luo et al. 2019b), where δ_N is a positive constant as given in the appendix and δ_N/PV_y represents the nonlinearity; $M_0 = \psi_{\max}/(2\sqrt{2/L_y})$ denotes the amplitude of blocking, with $\psi_{\max}$ and L_y representing the maximum streamfunction anomaly and meridional scale of blocking anomaly respectively. We can calculate $\psi_{\max}$ using the maximum amplitude of blocking anticyclonic anomaly. When the blocking amplitude M_0 is small, $C_N = -\delta_N M_0^2/(2k\mathrm{PV}_y)$ is small such that $C_{\mathrm{NP}} \approx C_P$. In this case, Eq. (4) reduces to Eq. (3). When the blocking amplitude M_0 is not small, the amplitude of blocking can influence the propagation. In this case, the role of PV_y in $C_N = -\delta_N M_0^2/(2k\mathrm{PV}_y)$ is opposite to that of PV_y in $-[\mathrm{PV}_y/(k^2 + m^2 + F)]$. This explains why large-amplitude blocking always moves westward (Luo 2000; Yao et al. 2017). In the linear phase speed formula Eq. (3), a small PV_y tends to favor the eastward propagation of blocking. In contrast, in the nonlinear phase speed formula Eq. (4), a small PV_y favors the retrogression of blocking even in the small blocking amplitude limit.

Brought to you by UNIVERSITETSBIBLIOTEKET I | Unauthenticated | Downloaded 03/09/22 08:50 AM UTC

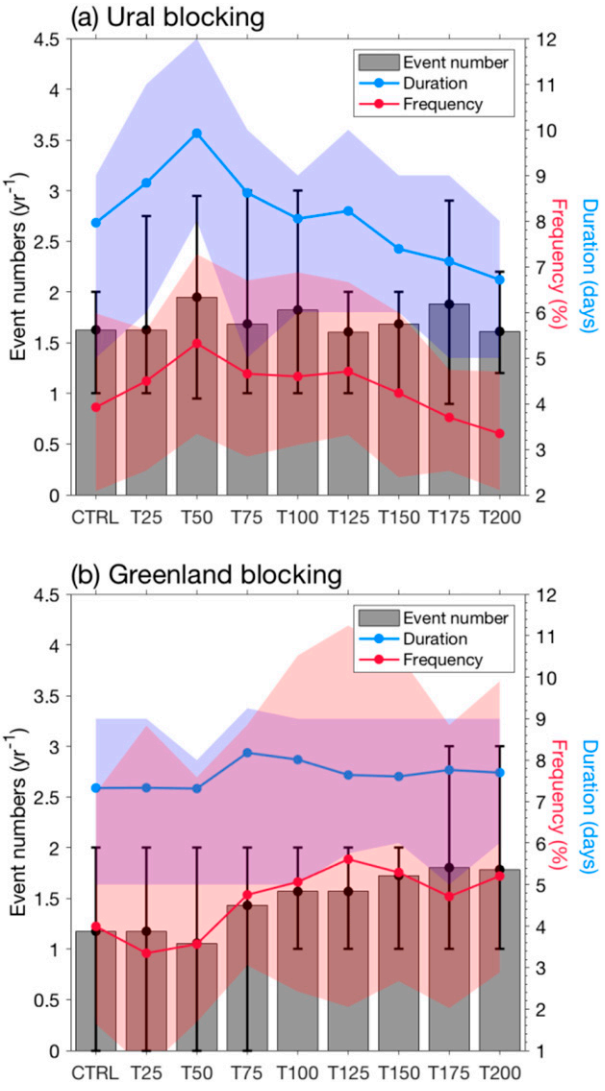

FIG. 5. Frequency, event duration, and event number of (a) UB and (b) GB as a function of the strength of BKS warming. Red shading with dots represents the domain-averaged blocking frequency averaged over 30°–90°E, 50°–75°N for UB and 90°–30°W, 50°–75°N for GB (%), blue shading with dots represents the event duration (days), and gray bars denote the event number per winter. Interquartile ranges are given by color shadings and whiskers. The duration differences between CTRL and other experiments in (a) are significant at the 95% confidence level using the Student's test, except for T100 and T125; also, the event number differences between CTRL and other experiments in (b) are also statistically significant, except for T25 and T50.

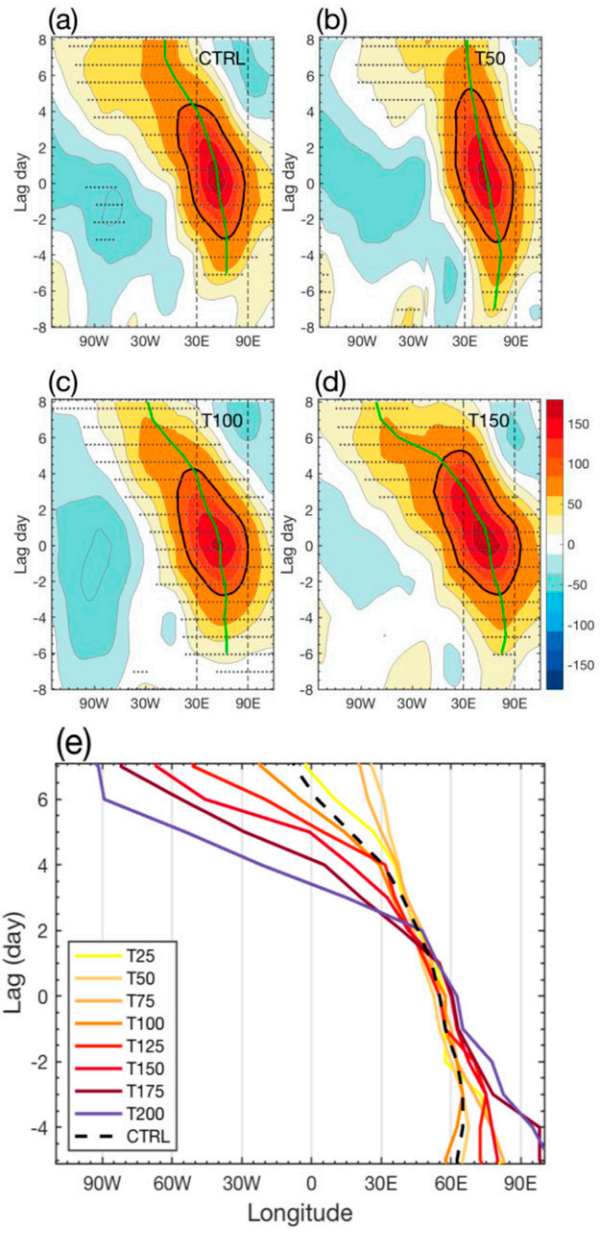

FIG. 6. Time–longitude evolution of composited daily Z500 anomalies (color shadings; CI = 20 gpm) averaged over 50°–75°N for the UB events in (a) CTRL, (b) T50, (c) T100, and (d) T150. (e) Longitudinal location of the daily maximum Z500 anomaly as a function of time for each experiment. Lag 0 denotes the peak day and negative lag days refer to days prior to the peak of UB event. In (a)–(d), the black thick line denotes the value of 100 gpm, and the green line denotes the daily trajectory of the maximum Z500 anomaly for UB events. Stippling denotes the statistically significant region at the 95% confidence level using the Student's t test.

b. *Response of background circulation to BKS warming*

As noted above, while most of the parameters in Eqs. (3) and (4) are constant across the experiments, the upstream background zonal wind (U) and the associated meridional background potential vorticity gradient (PV_y) are two critical factors influencing the propagation of UB. Thus, we calculate the DJF-mean response of U and PV_y, as well as the corresponding response of geopotential height at the 500-hPa level. Here we remove blocking days from lag −10 to 10 days before calculating the DJF-mean states to exclude the influence of UB events on the DJF-mean background state.

Brought to you by UNIVERSITETSBIBLIOTEKET I | Unauthenticated | Downloaded 03/09/22 08:50 AM UTC

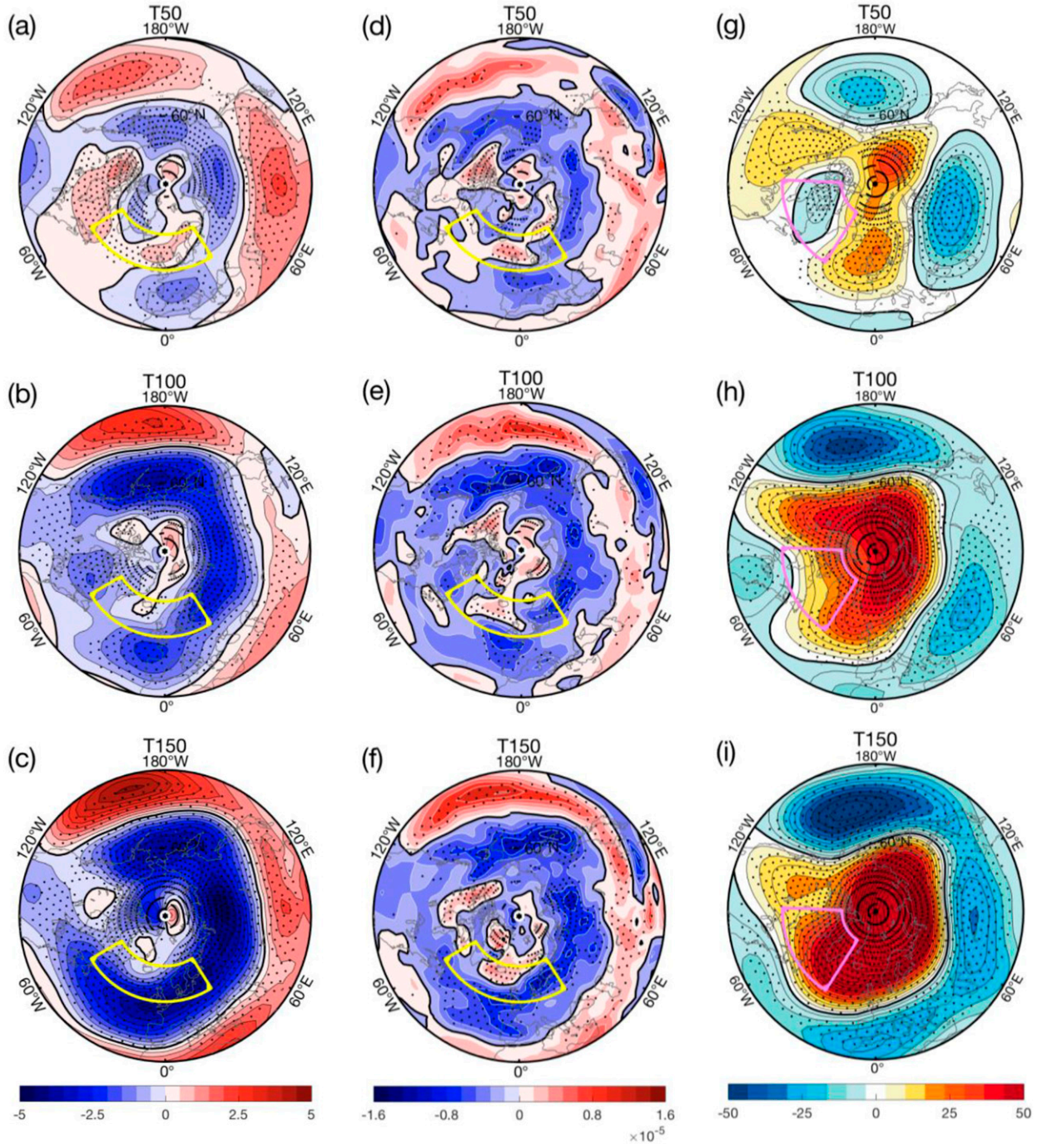

FIG. 7. DJF-mean (a)–(c) U500, (d)–(f) 500-hPa PV_y, and (g)–(i) Z500 response for (top) T50, (middle) T100, and (bottom) T150 compared to CTRL. These figures are plotted with color shading and contours with a thick zero line and CI = 0.5 m s^{-1} in (a)–(c), CI = 2×10^{-6} PVU m^{-1} (1 PVU = 10^{-6} m^2 s^{-1} K kg^{-1}) in (d)–(f), and CI = 10 gpm in (g)–(i). In the DJF-mean fields, the days from lag −10 to lag 10 have been removed for each UB event, where lag 0 denotes its peak day. The area of 60°W–30°E, 50°–70°N (90°–30°W, 50°–75°N) is marked by the yellow (violet) box. Stippling denotes the statistically significant region at the 95% confidence level using the Student's *t* test.

The responses of background states for T50, T100, and T150 are shown in Fig. 7. It is found that for a weak warming case (top of Fig. 7), the background U (Fig. 7a) and PV_y (Fig. 7d) decrease north of 50°N, especially in the east of 60°E over Eurasia, but increase slightly over the North Atlantic and Europe (yellow box in Fig. 7), which corresponds to a wave train in Z500 response (Fig. 7g). This wave train is characterized by a negative Z500 response in the northeast of North

Brought to you by UNIVERSITETSBIBLIOTEKET I | Unauthenticated | Downloaded 03/09/22 08:50 AM UTC

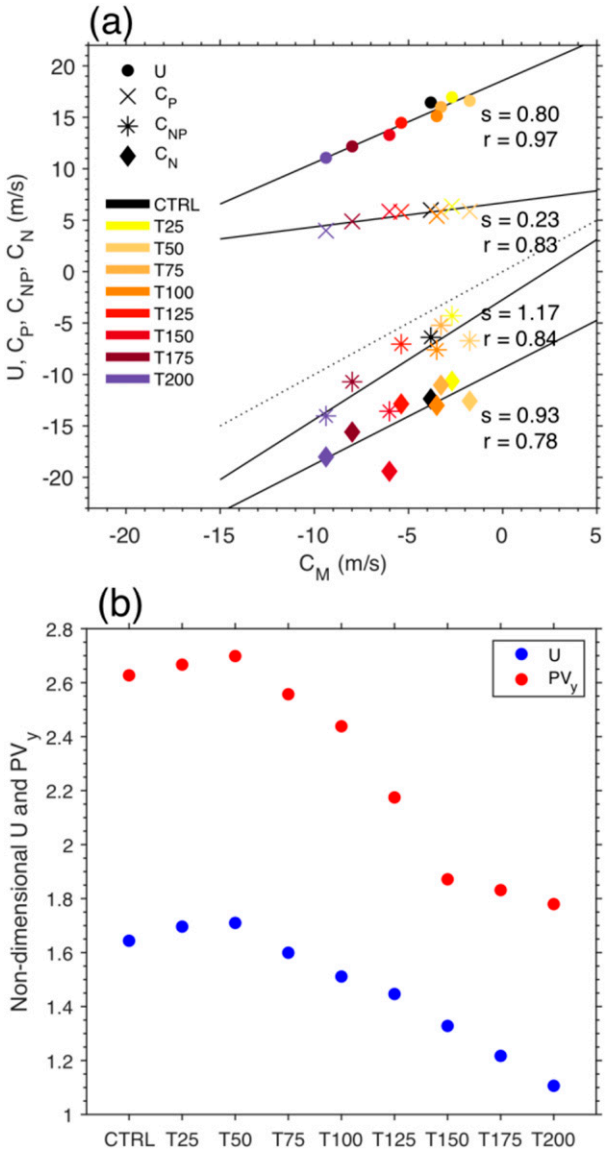

FIG. 8. (a) Scatterplots of U500 (dot), C_P (cross), C_{NP} (star), and C_N (diamond) that are calculated from Eqs. (3) and (4) against the time-mean propagation speed C_M of the composite UB event for each individual experiment. The black solid line denotes the linear regression with the slope denoted by the value of s. The value of r represents the correlation coefficient, whereas the dotted line denotes the line with a ratio of one. (b) Nondimensional DJF-mean U and PV_y averaged over 60°–30°E, 50°–75°N on the upstream side of Eurasia against the strength of BKS warming. To compare U and PV_y, here U is nondimensionalized by the characteristic wind speed 10 m s^{-1} and PV_y is nondimensionalized by the scale of 10^{-11} m^{-1}.

America or over North Atlantic high latitudes (the violet box in Fig. 7) and a positive Z500 response over northern Europe. For less strong (middle of Fig. 7) and strong (bottom of Fig. 7) BKS warming, a strong positive Z500 response appears over the entire Arctic region (Figs. 7h,i), which intensifies with the BKS warming and extends toward the North Atlantic mid-to-high latitudes so that the negative Z500 response in the northeast side of North America disappears for the weak forcing cases. Associated with the change of Z500, a circumpolar anomalous easterly is gradually built in mid-high latitudes (Figs. 7b,c). Correspondingly, the background U and PV_y are weakened in the broad region from North Atlantic to Eurasia. For these two cases, the background circulation response resembles a negative Arctic Oscillation (AO^-) or a negative NAO (NAO^-). Below, we will quantitatively examine the link between UB propagation and the background U and PV_y.

c. *Propagation of UB and its linkage with the background flow change*

This subsection mainly estimates the propagation speed of the simulated UB event and compare it with the theoretical prediction based on linear and nonlinear phase speed formulas presented in Eqs. (3) and (4). For each experiment, the daily phase speed of the composite UB event is estimated by calculating the zonal distance that its maximum Z500 anomaly travels per day as shown in Fig. 6e, and then we take the time average of the daily phase speed of UB from lag −6 to 6 days as its time-mean propagation speed C_M. In estimating the theoretical phase speeds C_P and C_{NP}, we consider the U and PV_y without UB events averaged over 60°W–30°E, 50°–75°N (yellow box in Fig. 7) as the upstream background U and PV_y in Eqs. (3) and (4), but the following results are not strongly altered by the size of the averaging area. The Z500 anomaly at 60°N is used as the value of $Z500_{max}$ to calculate $M_0 = \psi_{max}/(2\sqrt{2/L_y})$ through the relationship $\psi_{max} = Z500_{max}g/f$ (where $g = 9.8\,\mathrm{m\,s^{-2}}$ and f is the Coriolis parameter) because the maximum amplitude of the UB is typically centered at about 60°N. The blocking amplitude in Eqs. (3) and (4) is estimated by taking the time mean of the daily M_0 during the mature phase of UB (from lag −3 to 3 days). On this basis, one can obtain the theoretical phase speeds C_P and C_{NP} using the upstream background circulation and the blocking amplitude.

We show the relationship of the upstream zonal wind (U), the linear phase speed (C_P), the nonlinear phase speed (C_{NP}), and the nonlinear term of C_{NP} (C_N) against the mean propagation speed (C_M) of the simulated UB in a scatterplot (Fig. 8a). The U and C_P show strong positive correlations of 0.97 and 0.83 with the simulated mean propagation speed C_M, respectively. However, the values of U and C_P are positive (eastward), so that they cannot explain the westward propagation of UB. We can see that C_{NP} is closer to C_M because the stars in Fig. 8a are very close to the ideal one-to-one line (dotted line), and all the values of C_{NP} are negative. Moreover, the linear regression of C_{NP} against C_M shows a slope of 1.17 that is very close to one, whereas the slopes for U and C_P are smaller than one, suggesting that they underestimate the change of C_M, especially for C_P. Therefore, the nonlinear phase speed C_{NP} can better explain the UB propagation in our experiments.

We divide C_{NP} into a linear part C_P and a nonlinear part C_N. The regression slope of C_N against C_M is 0.93, which is much closer to one than that of C_P. In other words, the nonlinear component of C_{NP} plays a more important role than its linear component in representing the propagation speed of UB. The

Brought to you by UNIVERSITETSBIBLIOTEKET I | Unauthenticated | Downloaded 03/09/22 08:50 AM UTC

change of C_N is mainly determined by the change of PV_y because of $C_N = -\delta_N M_0^2/(2k\mathrm{PV}_y)$ as noted above, when M_0 changes small with BKS warming. However, the change of C_P is a total effect of the changes in U and PV_y whose effects on C_P are opposite as in Eq. (3). Nondimensional U and PV_y are analyzed to compare their responses to different strengths of BKS warming (Fig. 8b). It is found that nondimensional PV_y (red dots) is more sensitive to the strengthening of BKS warming than the nondimensional U (blue dots). Particularly, PV_y drops rapidly from T50 to T150 and becomes very small in T150, T175, and T200, resulting in a large negative C_{NP} and a strong westward propagation of UB.

The weakening of upstream zonal wind U and PV_y caused by strong BKS warming would favor the westward propagation of UB, corresponding to an emerging NAO^- response. Thus, we need to explore why the Z500 response around Greenland changes from negative to positive as BKS warming increases and what slows down the background zonal flow under a strong BKS warming. The NAO^- following Arctic sea ice loss has been suggested as a consequence of the downward propagation of the weakened stratospheric vortex (Baldwin and Dunkerton 2001; Kim et al. 2014; Sun et al. 2015; Zhang et al. 2018b); thus, it is likely that the early winter BKS warming modifies the North Atlantic circulation through the downward influence of the stratosphere. In the next section, we will investigate whether and how the stratospheric processes interfere with the background flow and UB propagation using two sets of nudging experiments.

5. Role of stratospheric processes in changing the North Atlantic circulation and UB

To examine whether the stratospheric signal can propagate to the troposphere and influence the North Atlantic when the BKS warming is strong, we show the time–pressure evolution of geopotential height response averaged over the polar cap (north of 65°N) and time series of domain-averaged daily Z500 response averaged over Greenland (90°–30°W, 50°–75°N; violet box in Fig. 7) in Fig. 9. It is found that the zonal-mean height response is intensified in the stratosphere and extends downward when the strength of BKS warming increases (Figs. 9a–c), implying that the stratospheric response may have a stronger impact on the tropospheric circulation when BKS warming is more intense. For a weak BKS warming, the coupling between the stratosphere and troposphere is weak in November (Fig. 9a). When the BKS warming is stronger, a significant troposphere–stratosphere coupling occurs in November and December, and the following significant tropospheric responses can persist throughout the winter (Figs. 9b,c). The stratosphere–troposphere coupling due to Arctic sea ice loss has been found in previous studies (e.g., Kim et al. 2014; Hoshi et al. 2019). Our results suggest that the stratosphere–troposphere coupling intensifies with the increasing strength of BKS warming and influences winter tropospheric circulation when BKS warming is strong.

Moreover, we calculate the domain-averaged Z500 response in the North Atlantic high latitudes (the violet box in Fig. 7) and show the results in Figs. 9d–f. It is found that there is no significant Z500 response over Greenland during the period from late November to March for weak BKS warming (Fig. 9d), whereas significant positive Z500 responses are seen during the winter for less strong and strong BKS warming (Figs. 9e,f). Especially for T150, the positive Z500 response grows in December and peaks in early January (Fig. 9f), associated with a prior downward propagation seen in Fig. 9c. Thus, the generation of the positive Z500 response in North Atlantic high latitudes is likely related to the downward propagation of the stratospheric positive geopotential height responses that results from strong BKS warming. Many previous studies also pointed out that the tropospheric response to a weakened stratospheric vortex occurs mainly in the North Atlantic (e.g., Baldwin and Dunkerton 2001; Kim et al. 2014).

We further conduct two sets of nudging experiments to explicitly quantify the Z500 response to different strengths of BKS warming when the stratosphere–troposphere coupling is included or excluded. Figures 10a–c show the DJF-mean Z500 responses for only considering the role of the tropospheric process, whereas Figs. 10d–f are the results considering the downward effect of the stratospheric processes only. Here, the DJF-mean Z500 response represents the deviation from that in CTRL_N. When the stratosphere–troposphere coupling is numerically suppressed via nudging (Figs. 10a–c) in all three forcing cases, we can find a negative Z500 response in the northeast of North America and two positive Z500 responses in the Eurasian high latitudes and in the east of North Atlantic midlatitudes, resembling the Z500 response in T50 (Fig. 7g). Between the negative and positive Z500 responses, anomalous southwesterly winds are expected to appear (not shown). The magnitude of the negative Z500 response around Greenland changes little with the strength of BKS warming. However, when we only consider the downward effect of stratospheric processes, the Z500 response turns to be an AO^--like pattern (Figs. 10d–f), and the magnitude of this AO^- pattern intensifies with the increasing strength of BKS warming. Weakened westerly winds in North Atlantic mid-high latitudes can be expected as the AO^- intensifies (not shown). The sum of the tropospheric process and the stratospheric process (Fig. S7) is similar to the full response to BKS warming (Figs. 7g–i), indicating the approximately linear additivity of the tropospheric dynamics and stratosphere–troposphere coupling.

In Fig. 11, we summarize the relative contribution of tropospheric and stratospheric processes to the DJF-mean Z500 response around Greenland (violet box in Fig. 10). The tropospheric process leads to a decrease of the Z500 anomaly over North Atlantic (blue bar), whereas the stratospheric process causes its increase (red bar), irrespective of BKS warming strength. When the combined effect of tropospheric and stratospheric processes is considered (green bar), the Z500 response in the North Atlantic high latitudes changes from negative to positive as the BKS warming intensifies, which is comparable to the total Z500 response in the experiments without nudging (white bar). In the case of weak BKS warming, the negative Z500 response associated with the tropospheric process (T50_T) is larger than the positive Z500 response associated with the stratospheric process (T50_S), resulting in a weak negative response in total. However, the negative response due to the tropospheric process gently strengthens as BKS warming increases. Thus, the rapidly magnifying

Brought to you by UNIVERSITETSBIBLIOTEKET I | Unauthenticated | Downloaded 03/09/22 08:50 AM UTC

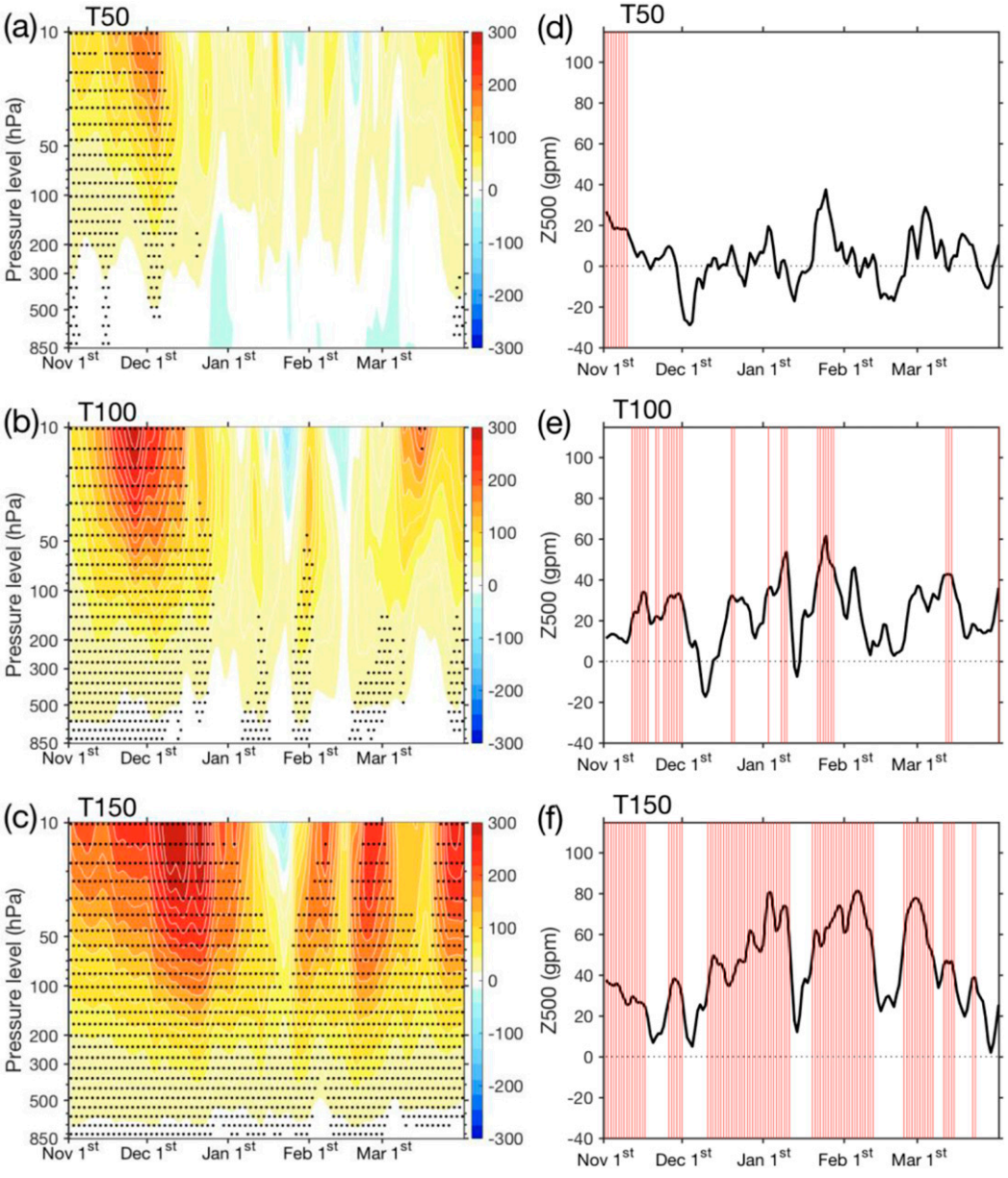

FIG. 9. (left) Time–vertical evolution of responded geopotential height anomaly that averaged over the polar cap (north of 65°N) and (right) time series of domain-averaged corresponding daily Z500 anomaly around Greenland (90°–30°W, 50°–75°N; as denoted by the violet box in Fig. 7) for (a),(d) T50, (b),(e) T100, and (c),(f) T150. Stippling in (a)–(c) and red shading in (d)–(f) reflects the statistical significance at the 95% confidence level using the Student's *t* test.

stratospheric downward influence can overcome the negative response, thus resulting in a positive response in total that corresponds to the AO^- pattern in Figs. 7 and 10.

The above results indicate that the interference of the stratospheric downward influence on the tropospheric circulation is essential in explaining the weakening of the North Atlantic mid-high latitude westerly winds under strong BKS warming, which may favor the westward propagation of UB. We examine the time–longitude evolution of composite daily Z500 anomalies averaged over 50°–75°N of the UB events for T50_T, T100_T, and T150_T in Fig. 12. A comparison with Figs. 6b–d reveals that, as expected, the westward propagation of UB becomes very small in the absence of stratospheric interference. This further confirms that stratospheric downward influence is crucial for explaining the nonlinear response of the UB propagation and persistence to BKS warming.

Brought to you by UNIVERSITETSBIBLIOTEKET I | Unauthenticated | Downloaded 03/09/22 08:50 AM UTC

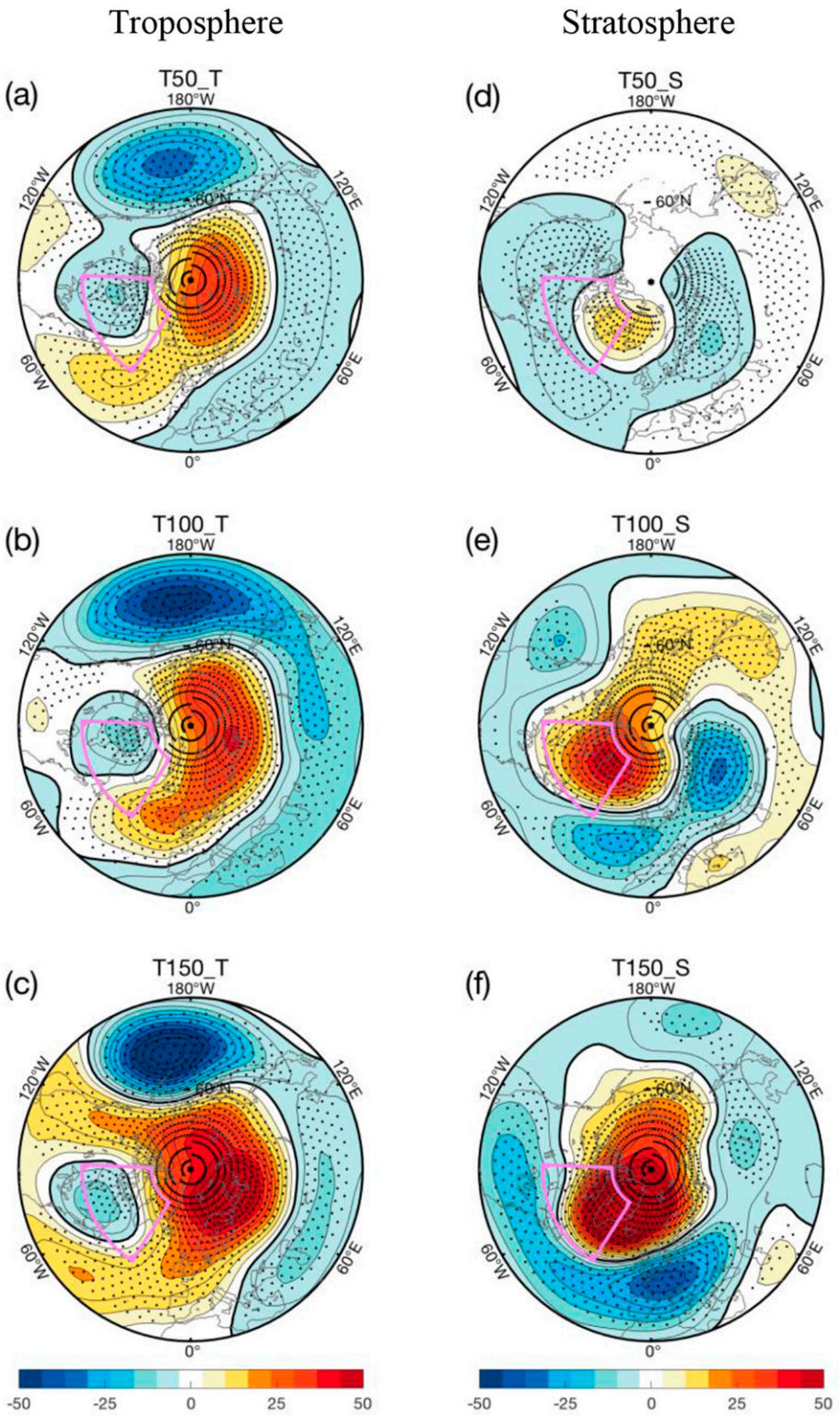

FIG. 10. DJF-mean Z500 responses with color shading (CI = 10 gpm) for nudging experiments (a)–(c) with the tropospheric process only and (d)–(f) with the downward influence of stratospheric processes only. The area of 90°–30°W, 50°–75°N is highlighted by the violet box. Stippling denotes the statistically significance region at the 95% confidence level using the Student's *t* test.

Brought to you by UNIVERSITETSBIBLIOTEKET I | Unauthenticated | Downloaded 03/09/22 08:50 AM UTC

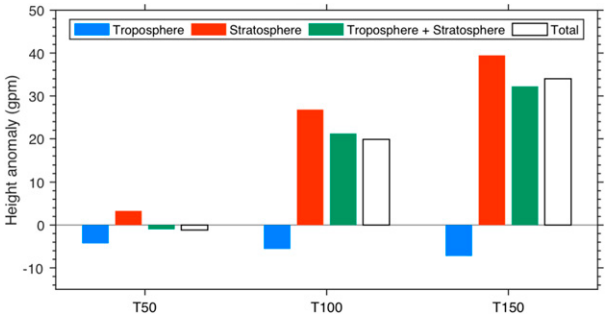

FIG. 11. DJF-mean Z500 anomaly response averaged over the North Atlantic high latitudes (the violet box in Fig. 10) in the nudging experiments with the tropospheric process only (blue bar), with the downward influence of stratospheric processes only (red bar) and their sum (green bar) for strong (T150), medium (T100), and weak (T50) BKS warming cases (bars from left to right). The white bar denotes the total response to BKS warming without nudging in the T50, T100, and T150 experiments.

6. Conclusions and discussion

In this study, we have used a dry dynamic core model to examine the Ural blocking (UB) response to Barents–Kara Seas (BKS) warming with different strengths. It is found that the strength of BKS warming mainly affects the propagation and local persistence of UB events by modifying its upstream background tropospheric circulation. As summarized in a schematic in Fig. 13, the tropospheric background circulation response to a weak BKS warming leads to a less westward movement and an increased duration of UB, while in this case the effect of stratospheric processes is negligible. When BKS warming is strong, the stratospheric polar vortex weakens significantly due to the increased propagation of the upward planetary waves and accompanies a downward propagation that generates an NAO^- response and reduces the upstream westerly winds and meridional potential vorticity gradient in the North Atlantic and European mid-high latitudes, thereby resulting in an increased westward propagation and a shortened duration of UB. In summary, the tropospheric (stratospheric) process plays a dominant role in the UB change when BKS warming is weak (strong) (Fig. 13).

As a result, the UB shows a nonlinear nonmonotonic change for a linear increase in BKS warming. When BKS warming is weak, UB becomes quasi-stationary and locally persistent due to strengthened North Atlantic mid-high-latitude westerly winds. When BKS warming is strong, the positive response of blocking frequency shifts to the North Atlantic and the westward propagation of UB is enhanced due to weakened North Atlantic and European mid-high-latitude westerly winds associated with the NAO^- response. We have explained how the weakened upstream background U and PV_y affect the UB propagation using the nonlinear phase speed formula of atmospheric blocking (Luo et al. 2019b). It is revealed that the propagation speed of UB can be well explained by the nonlinear phase speed C_{NP} of blocking wave packet, and the nonlinear part of C_{NP} dominates the westward propagation of UB, emphasizing the importance of the upstream PV_y in changing the movement of UB.

In conclusion, we find that the different strength of BKS warming leads to nonmonotonic and nonlinear changes of the UB and tropospheric background circulation, and we propose a mechanism to explain it. The mechanism mainly involves a balance between the stratospheric influence and the tropospheric influence on the tropospheric circulation over North Atlantic mid-high latitudes. Our simulations with weak BKS warmings corroborate the observational findings in Yao et al. (2017) and Luo et al. (2018) that weak BKS warming favors persistence and quasi-stationarity of the UB. However, we further reveal that the UB tends to be westward-shifting when BKS warming is strong, thus explaining why the UB in December 2011 shifts westward under extremely low BKS sea ice. The nonlinear response of UB is closely related to the mean-state tropospheric circulation response over North

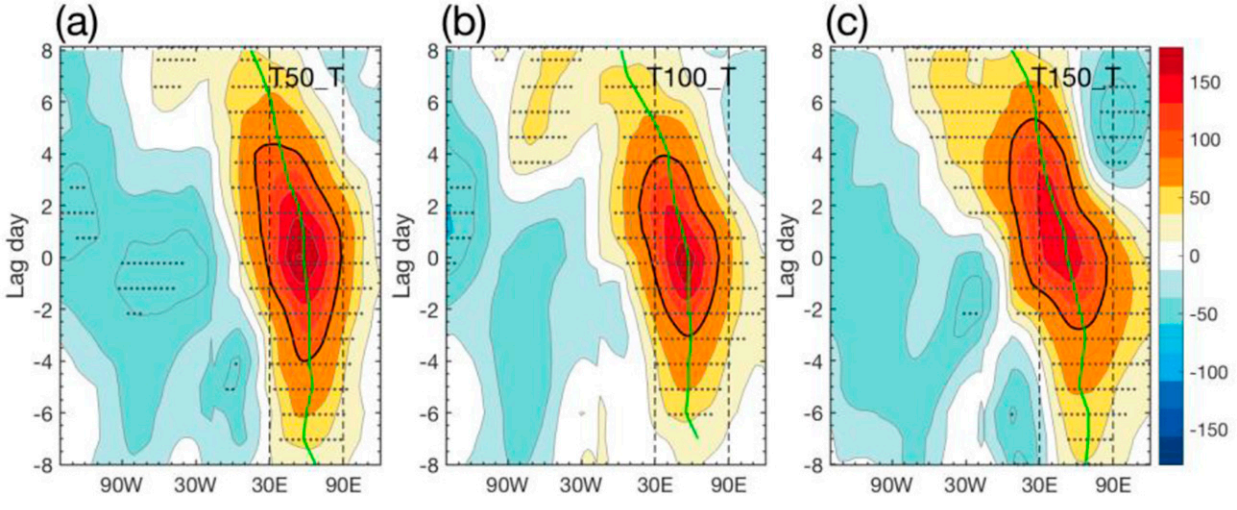

FIG. 12. As in Figs. 6b–d, but for (a) T50_T, (b) T100_T, and (c) T150_T, which are three nudging experiments with the tropospheric process only.

Brought to you by UNIVERSITETSBIBLIOTEKET I | Unauthenticated | Downloaded 03/09/22 08:50 AM UTC

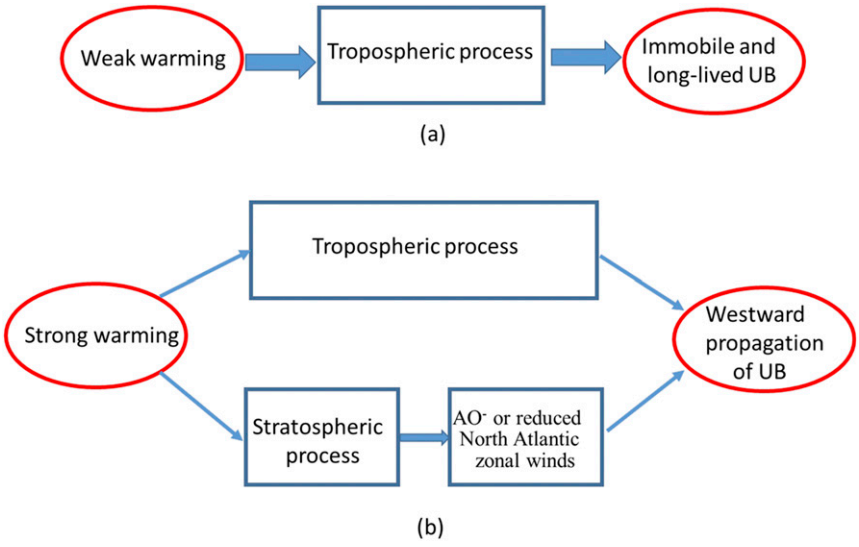

FIG. 13. Schematic diagram of two scenarios of BKS warming affecting the UB propagation: (a) a scenario with tropospheric process only for weak BKS warming and (b) a more complicated scenario that induces the tropospheric and stratospheric processes for strong BKS warming. In the second scenario with strong BKS warming, the weakened stratospheric polar vortex propagates downward and induces an AO^{-} response, resulting in weakened westerly winds in the North Atlantic mid-high latitudes and thus favoring the notable westward propagation of UB, less local persistent UB, and fewer blocked days over the UB region. The stratospheric process dominates the North Atlantic circulation when BKS warming is strong, whereas the tropospheric process dominates when BKS warming is weak.

Atlantic. Our results also support the findings of Petoukhov and Semenov (2010). They noted that the atmospheric circulation over Eurasia changes from an anticyclonic anomaly to a cyclonic anomaly when the BKS SIC drops from 100%–80% to 80%–40% with the European Centre Hamburg Atmosphere Model ECHAM5. In addition, we also further identify the importance of the stratospheric pathway in modifying the tropospheric mean-state over the North Atlantic and the nonlinear response of UB to BKS warming.

Our results emphasize another degree of complexity in the linkage between the Arctic and midlatitudes. The impact of the Arctic sea ice loss and Arctic amplification on the midlatitude circulation likely depends on the magnitude of the forcing due to strong nonlinearity in the mid- to high-latitude atmospheric dynamics and the stratosphere–troposphere coupling, which might be responsible for some of the discrepancies found in previous studies. Caution is advised in interpreting the statistical results using linear analysis and the modeling results with a single forcing magnitude.

Acknowledgments. The authors thank Zheng Wu, Thomas Reichler, Mingfang Ting, and Peter Siew for helpful discussions. This work is supported by the Chinese Academy of Sciences Strategic Priority Research Program (Grant XDA19070403), the National Natural Science Foundation of China (Grants 41790473), and the National Key Research and Development Program of China (2016YFA0601802). Xiaodan Chen acknowledge project funding by the China Postdoctoral Science Foundation (BX20200087). Yutian Wu acknowledges the support from the U.S. National Science Foundation (AGS-1815138) and the Lamont Center for Climate and Life fellowship. Jian Lu is supported by the Regional and Global Climate Modeling Program of U.S. Department of Energy Office of Science. The Pacific Northwest National Laboratory is operated for the Department of Energy by Battelle Memorial Institute under contract DE-AC05-76RL01830.

APPENDIX

Coefficients in the Nonlinear Phase Speed Eq. (4)

For a dimensional nonlinear phase speed in Eq. (4),

$$\delta_N = \frac{km\sum_{n=1}^{\infty} q_n g_n^2 [k^2 + m^2 - m^2(n+0.5)^2]}{k^2 + m^2 + F}$$

is a constant nonlinear parameter in experiments,

$$q_n = \frac{4k^2 m}{L_y\left\{1 - \frac{(m^2 + F - k^2)[F + m^2(n+0.5)^2]}{(k^2 + m^2 + F)^2}\right\}},$$

$g_n = 8/\{mL_y[4 - (n + 0.5)^2]\}$, $k = 2\pi/L_x$, $m = -2\pi/L_y$, L_x and L_y are the zonal and meridional wavelengths of the blocking wave, $L_x = 2\pi r_0 \cos\phi/n$ with a zonal wavenumber of integer n, and Earth's radius $r_0 = 6371$ km. Here we choose $L_y = 5000$ km,

Brought to you by UNIVERSITETSBIBLIOTEKET I | Unauthenticated | Downloaded 03/09/22 08:50 AM UTC

$\phi_0 = 60°$N, and $n = 2$ to represent the typical shape and location of Ural blocking; also, $F = 1/R_d^2$, where R_d is the radius of Rossby deformation. The derivation of C_{NP} can be found in Luo et al. (2019a,b).

REFERENCES

Baldwin, M. P., and T. J. Dunkerton, 2001: Stratospheric harbingers of anomalous weather regimes. *Science*, **294**, 581–584, https://doi.org/10.1126/science.1063315.

Blackport, R., J. A. Screen, K. van der Wiel, and R. Bintanja, 2019: Minimal influence of reduced Arctic sea ice on coincident cold winters in mid-latitudes. *Nat. Climate Change*, **9**, 697–704, https://doi.org/10.1038/s41558-019-0551-4.

Chang, E. K. M., 2006: An idealized nonlinear model of the Northern Hemisphere winter storm tracks. *J. Atmos. Sci.*, **63**, 1818–1839, https://doi.org/10.1175/JAS3726.1.

Chen, X., D. Luo, S. Feldstein, and S. Lee, 2018: Impact of winter Ural blocking on Arctic sea ice: Short-time variability. *J. Climate*, **31**, 2267–2282, https://doi.org/10.1175/JCLI-D-17-0194.1.

Cohen, J., and Coauthors, 2014: Recent Arctic amplification and extreme mid-latitude weather. *Nat. Geosci.*, **7**, 627–637, https://doi.org/10.1038/ngeo2234.

——, and Coauthors, 2020: Divergent consensuses on Arctic amplification influence on midlatitude severe winter weather. *Nat. Climate Change*, **10**, 20–29, https://doi.org/10.1038/s41558-019-0662-y.

Dai, A., and M. Song, 2020: Little influence of Arctic amplification on midlatitude climate. *Nat. Climate Change*, **10**, 231–237, https://doi.org/10.1038/s41558-020-0694-3.

Dee, D. P., and Coauthors, 2011: The ERA-Interim reanalysis: Configuration and performance of the data assimilation system. *Quart. J. Roy. Meteor. Soc.*, **137**, 553–597, https://doi.org/10.1002/qj.828..

Deser, C., R. A. Tomas, and L. Sun, 2015: The role of ocean–atmosphere coupling in the zonal-mean atmospheric response to Arctic sea ice loss. *J. Climate*, **28**, 2168–2186, https://doi.org/10.1175/JCLI-D-14-00325.1.

Dunn-Sigouin, E., S.-W. Son, and H. Lin, 2013: Evaluation of Northern Hemisphere blocking climatology in the global environment multiscale model. *Mon. Wea. Rev.*, **141**, 707–727, https://doi.org/10.1175/MWR-D-12-00134.1.

Francis, J. A., and S. J. Vavrus, 2012: Evidence linking Arctic amplification to extreme weather in mid-latitudes. *Geophys. Res. Lett.*, **39**, L06801, https://doi.org/10.1029/2012GL051000.

Honda, M., J. Inoue, and S. Yamane, 2009: Influence of low Arctic sea-ice minima on anomalously cold Eurasian winters. *Geophys. Res. Lett.*, **36**, L08707, https://doi.org/10.1029/2008GL037079.

Hoshi, K., J. Ukita, M., Honda, T. Nakamura, K. Yamazaki, Y. Miyoshi, and R. Jaiser, 2019: Weak stratospheric polar vortex events modulated by the Arctic sea-ice loss. *J. Geophys. Res. Atmos.*, **124**, 858–869, https://doi.org/10.1029/2018JD029222.

Inoue, J., M. E. Hori, and K. Takaya, 2012: The role of Barents Sea ice in the wintertime cyclone track and emergence of a warm-Arctic cold-Siberian anomaly. *J. Climate*, **25**, 2561–2568, https://doi.org/10.1175/JCLI-D-11-00449.1.

Jucker, M., S. Fueglistaler, and G. K. Vallis, 2014: Stratospheric sudden warmings in an idealized GCM. *J. Geophys. Res. Atmos.*, **119**, 11 054–11 064, https://doi.org/10.1002/2014JD022170.

Kim, B. M., S. W. Son, S. K. Min, J. H. Jeong, S. J. Kim, X. Zhang, T. Shim, and J. H. Yoon, 2014: Weakening of the stratospheric polar vortex by Arctic sea-ice loss. *Nat. Commun.*, **5**, 4646, https://doi.org/10.1038/ncomms5646.

Kug, J.-S., J.-H. Jeong, Y.-S. Jang, B.-M. Kim, C. K. Folland, S.-K. Min, and S.-W. Son, 2015: Two distinct influences of Arctic warming on cold winters over North America and East Asia. *Nat. Geosci.*, **8**, 759–762, https://doi.org/10.1038/ngeo2517.

Liu, J., J. A. Curry, H. Wang, M. Song, and R. M. Horton, 2012: Impact of declining Arctic sea ice on winter snowfall. *Proc. Natl. Acad. Sci. USA*, **109**, 4074–4079, https://doi.org/10.1073/pnas.1114910109.

Luo, D., 2000: Planetary-scale baroclinic envelope Rossby solitons in a two-layer model and their interaction with synoptic-scale eddies. *Dyn. Atmos. Oceans*, **32**, 27–74, https://doi.org/10.1016/S0377-0265(99)00018-4.

——, 2005: A barotropic envelope Rossby soliton model for block–eddy interaction. Part I: Effect of topography. *J. Atmos. Sci.*, **62**, 5–21, https://doi.org/10.1175/1186.1.

——, Y. Xiao, Y. Yao, A. Dai, I. Simmonds, and C. L. E. Franzke, 2016: Impact of Ural blocking on winter warm Arctic–cold Eurasian anomalies. Part I: Blocking-induced amplification. *J. Climate*, **29**, 3925–3947, https://doi.org/10.1175/JCLI-D-15-0611.1.

——, X. Chen, A. Dai, and I. Simmonds, 2018: Changes in atmospheric blocking circulations linked with winter Arctic warming: A new perspective. *J. Climate*, **31**, 7661–7678, https://doi.org/10.1175/JCLI-D-18-0040.1.

——, ——, J. Overland, I. Simmonds, Y. Wu, and P. Zhang, 2019a: Weakened potential vorticity barrier linked to recent Arctic sea ice loss and midlatitude cold extremes. *J. Climate*, **32**, 4235–4261, https://doi.org/10.1175/JCLI-D-18-0449.1.

——, W. Zhang, L. Zhong, and A. Dai, 2019b: A nonlinear theory of atmospheric blocking: A potential vorticity gradient view. *J. Atmos. Sci.*, **76**, 2399–2427, https://doi.org/10.1175/JAS-D-18-0324.1.

Mori, M., M. Watanabe, H. Shiogama, J. Inoue, and M. Kimoto, 2014: Robust Arctic sea-ice influence on the frequent Eurasian cold winters in past decades. *Nat. Geosci.*, **7**, 869–873, https://doi.org/10.1038/ngeo2277.

——, Y. Kosaka, M. Watanabe, H. Nakamura, and M. Kimoto, 2019: A reconciled estimate of the influence of Arctic sea-ice loss on recent Eurasian cooling. *Nat. Climate Change*, **9**, 123–129, https://doi.org/10.1038/s41558-018-0379-3.

Nakamura, T., K. Yamazaki, K. Iwamoto, M. Honda, Y. Miyoshi, Y. Ogawa, Y. Tomikawa, and J. Ukita, 2016: The stratospheric pathway for Arctic impacts on midlatitude climate. *Geophys. Res. Lett.*, **43**, 3494–3501, https://doi.org/10.1002/2016GL068330.

Ogawa, F., and Coauthors, 2018: Evaluating impacts of recent Arctic sea ice loss on the Northern Hemisphere winter climate change. *Geophys. Res. Lett.*, **45**, 3255–3263, https://doi.org/10.1002/2017GL076502.

Outten, S. D., and I. Esau, 2012: A link between Arctic sea ice and recent cooling trends over Eurasia. *Climatic Change*, **110**, 1069–1075, https://doi.org/10.1007/s10584-011-0334-z.

Overland, J. E., and M. Wang, 2010: Large-scale atmospheric circulation changes are associated with the recent loss of Arctic sea ice. *Tellus*, **62A** (1), 1–9, https://doi.org/10.1111/j.1600-0870.2009.00421.x.

——, K. R. Wood, and M. Wang, 2011: Warm Arctic–cold continents: Climate impacts of the newly open Arctic Sea. *Polar Res.*, 15787, https://doi.org/10.3402/polar.v30i0.15787.

——, and Coauthors, 2015: The melting Arctic and mid-latitude weather patterns: Are they connected? *J. Climate*, **28**, 7917–7932, https://doi.org/10.1175/JCLI-D-14-00822.1.

——, and Coauthors, 2016: Nonlinear response of mid-latitude weather to the changing Arctic. *Nat. Climate Change*, **6**, 992–999, https://doi.org/10.1038/nclimate3121.

Brought to you by UNIVERSITETSBIBLIOTEKET I | Unauthenticated | Downloaded 03/09/22 08:50 AM UTC

Peings, Y., 2019: Ural blocking as a driver of early-winter stratospheric warmings. *Geophys. Res. Lett.*, **46**, 5460, https://doi.org/10.1029/2019GL082097.

——, and G. Magnusdottir, 2014: Response of the wintertime Northern Hemisphere atmospheric circulation to current and projected Arctic sea ice decline: A numerical study with CAM5. *J. Climate*, **27**, 244–264, https://doi.org/10.1175/JCLI-D-13-00272.1.

Petoukhov, V., and V. A. Semenov, 2010: A link between reduced Barents-Kara sea ice and cold winter extremes over northern continents. *J. Geophys. Res.*, **115**, D21111, https://doi.org/10.1029/2009JD013568.

Screen, J. A., and I. Simmonds, 2010: The central role of diminishing sea ice in recent Arctic temperature amplification. *Nature*, **464**, 1334–1337, https://doi.org/10.1038/nature09051.

——, and Coauthors, 2018: Consistency and discrepancy in the atmospheric response to Arctic sea-ice loss across climate models. *Nat. Geosci.*, **11**, 155–163, https://doi.org/10.1038/s41561-018-0059-y.

Semenov, V. A., and M. Latif, 2015: Nonlinear winter atmospheric circulation response to Arctic sea ice concentration anomalies for different periods during 1966–2012. *Environ. Res. Lett.*, **10**, 054020, https://doi.org/10.1088/1748-9326/10/5/054020.

Shepherd, T. G., 2016: Effects of a warming Arctic. *Science*, **353**, 989–990, https://doi.org/10.1126/science.aag2349.

Siew, P. Y. F., C. Li, S. P. Sobolowski, and M. P. King, 2020: Intermittency of Arctic-midlatitude teleconnections: Stratospheric pathway between autumn sea ice and the winter North Atlantic Oscillation. *Wea. Climate Dyn.*, **1**, 261–275, https://doi.org/10.5194/WCD-1-261-2020.

Simpson, I. R., P. Hitchcock, T. G. Shepherd, and J. F. Scinocca, 2013: Southern annular mode dynamics in observations and models. Part I: The influence of climatological zonal wind biases in a comprehensive GCM. *J. Climate*, **26**, 3953–3967, https://doi.org/10.1175/JCLI-D-12-00348.1.

Smith, D. M., N. J. Dunstone, A. A. Scaife, E. K. Fiedler, D. Copsey, and S. C. Hardiman, 2017: Atmospheric response to Arctic and Antarctic sea ice: The importance of ocean–atmosphere coupling and the background state. *J. Climate*, **30**, 4547–4565, https://doi.org/10.1175/JCLI-D-16-0564.1.

Sun, L., C. Deser, and R. A. Tomas, 2015: Mechanisms of stratospheric and tropospheric circulation response to projected Arctic sea ice loss. *J. Climate*, **28**, 7824–7845, https://doi.org/10.1175/JCLI-D-15-0169.1.

——, J. Perlwitz, and M. Hoerling, 2016: What caused the recent "warm Arctic, cold continents" trend pattern in winter temperatures? *Geophys. Res. Lett.*, **43**, 5345–5352, https://doi.org/10.1002/2016GL069024.

——, M. Alexander, and C. Deser, 2018: Evolution of the global coupled climate response to Arctic sea ice loss during 1990–2090 and its contribution to climate change. *J. Climate*, **31**, 7823–7843, https://doi.org/10.1175/JCLI-D-18-0134.1.

Tang, Q., X. Zhang, X. Yang, and J. A. Francis, 2013: Cold winter extremes in northern continents linked to Arctic sea ice loss. *Environ. Res. Lett.*, **8**, 014036, https://doi.org/10.1088/1748-9326/8/1/014036.

Tyrlis, E., E. Manzini, J. Bader, J. Ukita, H. Nakamura, and D. Matei, 2019: Ural blocking driving extreme Arctic sea ice loss, cold Eurasia, and stratospheric vortex weakening in autumn and early winter 2016–2017. *J. Geophys. Res. Atmos.*, **124**, 11 313–11 329, https://doi.org/10.1029/2019JD031085.

——, J. Bader, E. Manzini, J. Ukita, H. Nakamura, and D. Matei, 2020: On the role of Ural blocking in driving the warm Arctic–cold Siberia pattern. *Quart. J. Roy. Meteor. Soc.*, **146**, 2138–2153, https://doi.org/10.1002/qj.3784.

Vihma, T., 2014: Effects of Arctic sea ice decline on weather and climate: A review. *Surv. Geophys.*, **35**, 1175–1214, https://doi.org/10.1007/s10712-014-9284-0.

Walsh, J. E., 2014: Intensified warming of the Arctic: Causes and impacts on middle latitudes. *Global Planet. Change*, **117**, 52–63, https://doi.org/10.1016/j.gloplacha.2014.03.003.

Wu, Y., and K. L. Smith, 2016: Response of Northern Hemisphere midlatitude circulation to Arctic amplification in a simple atmospheric general circulation model. *J. Climate*, **29**, 2041–2058, https://doi.org/10.1175/JCLI-D-15-0602.1.

Wu, Z., and T. Reichler, 2018: Towards a more Earth-like circulation in idealized models. *J. Adv. Model. Earth Syst.*, **10**, 1458–1469, https://doi.org/10.1029/2018MS001356.

Xu, X., S. He, Y. Gao, T. Furevik, H. Wang, F. Li, and F. Ogawa, 2019: Strengthened linkage between midlatitudes and Arctic in boreal winter. *Climate Dyn.*, **53**, 3971–3983, https://doi.org/10.1007/s00382-019-04764-7.

Yao, Y., D. Luo, A. Dai, and I. Simmonds, 2017: Increased quasi-stationarity and persistence of Ural blocking and Eurasian extreme cold events in response to Arctic warming. Part I: Insight from observational analyses. *J. Climate*, **30**, 3549–3568, https://doi.org/10.1175/JCLI-D-16-0261.1.

Yeh, T. C., 1949: On energy dispersion in the atmosphere. *J. Atmos. Sci..*, **6**, 1–16, https://doi.org/10.1175/1520-0469(1949)006<0001:OEDITA>2.0.CO;2.

Zhang, P., Y. Wu, I. Simpson, K. L. Smith, X. Zhang, B. De, and P. Callaghan, 2018a: A stratospheric pathway linking a colder Siberia to Barents-Kara sea ice loss. *Sci. Adv.*, **4**, eaat6025, https://doi.org/10.1126/sciadv.aat6025.

——, ——, and K. Smith, 2018b: Prolonged effect of the stratospheric pathway in linking Barents-Kara Sea sea ice variability to the midlatitude circulation in a simplified model. *Climate Dyn.*, **50**, 527–539, https://doi.org/10.1007/s00382-017-3624-y.

Brought to you by UNIVERSITETSBIBLIOTEKET I | Unauthenticated | Downloaded 03/09/22 08:50 AM UTC